Journal of Marine Research, 60, 47–72, 2002

The transport in the Ekman surface layer on the spherical Earth

by Nathan Paldor[1]

ABSTRACT

The modification of the transport in the Ekman layer on the *f*-plane due to the Coriolis parameter's variation with latitude and the curvature of Earth's surface is analyzed by considering the temporal changes in the angular momentum. The latter plays the role of a dynamical variable of the model, replacing the zonal velocity component, and drag is modeled by Rayleigh friction. The steady transport, which on an *f*-plane is perpendicularto the applied wind stress, is recovered on the Earth as a special solution where the meridional velocity is time-independent. For zonal wind stress, the trajectory on Earth is simply a great circle that passes through the poles while for meridional wind stress the special solution can have a time-independent nonzero meridional component so the trajectory does not have to be purely zonal. This asymmetry between zonal and meridional wind stresses on the Earth is due to the Coriolis parameter's variation with latitude only—an effect that is completely neglected on the *f*-plane.

For steady wind forcing, the dynamical system is three-dimensional and its fixed points are located at the latitudes of vanishing wind stress. In the drag-free case, when the curl of the wind stress does not vanish at the fixed points, these points are always unstable; namely there exists at least one repulsive direction in (the 3D) phase space. When drag is included, these steady states still prevail but become stable for realistic values of the wind forcing and drag. An additional steady state, located right on the equator, exists in this case and its zonal velocity attains a constant value determined by the balance between the applied stress and the drag force. Although drag is present, this steady state is unstable for negative wind stress (i.e. easterly winds) so any deviation from a purely westward, equatorial, trajectory will grow exponentially in time. Naturally, no similar instability of the steady states occurs on the *f*-plane.

The curl of the zonal wind stress at the latitudes where the stress itself vanishes determines the trajectory of a water column originating there via the nonlinear interaction between the motion due to inertial oscillations and that due to the wind-forced changes of the angular momentum.

Temporal or zonal dependence of the wind stress has a profound effect on the trajectories, especially near the unstable latitudes due to the increase in the dimensionality of the system that enables more complex trajectories. The present simple model can quantitatively reproduce the observed fast dispersal of nearby launched drifters with steady and smooth wind stress. It can also explain qualitatively the different spectra of clusters of drifters launched in two field experiments in the NE Pacific Ocean under similar winds and the highly variable angle between the wind and the observed trajectories of clusters of drifters.

1. Ring Department of Atmospheric Sciences, The Hebrew University of Jerusalem, Jerusalem, 91904, Israel.
email: nathan.paldor@huji.ac.il

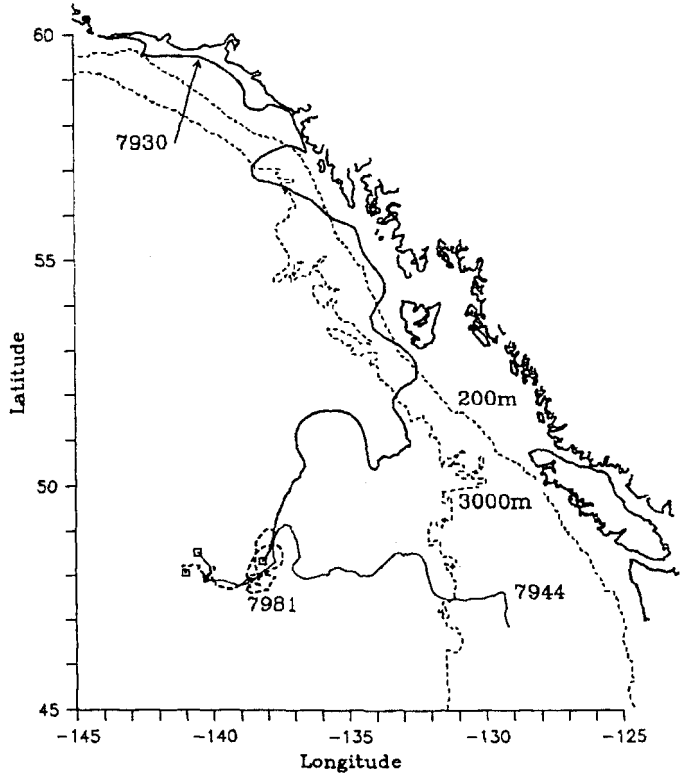

Figure 1. Observation of the trajectories of three drifters launched in the northwest Pacific Ocean during the first week of October 1987. On the 10th of October, the three drifters came within 200 km of one another and during the following 164 days one drifter moved less than 100 km, a second one moved 850 km eastward and the third drifter traveled 1000 km northward. On the *f*-plane this can only be explained as a result of high short-scale (in time and/or space) variability of the wind stress. Reproduced by permission of the American Meteorological Society.

1. Introduction

This study is motivated by recent observations of the fast dispersal of trajectories of drogued drifters in the ocean's surface such as that documented in Paduan and Niiler (1993; Fig. 4), shown here as Figure 1. Three TRISTAR drifters (drogued at 15 m) that had been launched in early October 1987 within 1 week and 200 km of each other, converged to a distance of about 100 km of each other on 10/Oct./87. In the subsequent 164 days, drifter #7930 traveled about 1000 km northward, drifter #7944 traveled about 850 km eastward while drifter #7981 hardly moved at all from its launch site. Such dramatic dispersal of nearby trajectories is typical of chaotic dynamics where phase space orbits can diverge exponentially. Yet, the existing theory of transport in the Ekman layer is linear (*f*-plane), which implies that the only way for it to be relevant to these drifter observations is for the wind stress (i.e. the forcing term) to vary wildly on short time and length scales.

We seek an alternate theory that can account for these observations by including nonlinear dynamics on the Earth but with smooth (in space) and time-independent wind stress. The theory developed here is an extension of the *f*-plane model to the Earth where the Coriolis parameter, and in accordance with it the wind stress too, vary in space. As in the *f*-plane model, drag is modeled by Rayleigh friction but on the Earth, the Ekman layer dynamics is chaotic. Additional features of drifter trajectories, not fully explained based on *f*-plane dynamics, are addressed in the Discussion section and the present theory suggests that these, too, can be explained on the Earth. The *f*-plane model and the essential elements in its extension to the Earth are reviewed next.

a. Ekman transport on the f-plane

The observation of inertial currents in the mixed layer was successfully simulated with "striking accuracy" (Pollard and Millard, 1970; PM70, hereafter) by a linear model on the *f*-plane in which the time-dependent wind stress is uniformly distributed over the entire surface mixed layer and drag is modeled by Rayleigh friction. The same model was employed to simulate observations of moored current meters in other locations (Kundu, 1976; Käse and Olbers, 1979) and these simulations, too, resulted in qualitatively satisfactory currents. It is explicitly assumed in these studies that the mixed layer is turbulently homogenized so the horizontal velocity there is uniform, and changes in the wind stress are instantaneously transmitted to its entire depth. This implies that the current's forcing at any depth within the mixed layer is given by the wind stress divided by the depth of the mixed layer. A model of wind-driven transport, i.e. vertically integrated horizontal velocity in the mixed layer, obeys the same equations (Gill, 1982) but with the forcing provided by the wind stress itself instead of the wind stress divided by the mixed-layer depth.

These simulations (and observations) focused on the temporal changes in the current at a particular station when the water is forced by the observed wind stress. However, they provide no information on the current's spatial distribution and on the trajectory of a tagged water column when the wind stress is not spatially uniform, which is the goal of drifter tracking.

b. An outline of the main modifications to the f-plane Ekman model

The present study employs an angular momentum-based, Lagrangian, version of the local, *f*-plane, PM70 model to simulate the large-scale trajectories of water columns in the mixed layer. While in PM70 the observed, time-dependent, wind stress is assumed uniform in space, the present work considers the complementary case where the wind stress is time-independent but varies spatially. To be consistent with the inclusion of the wind stress' spatial variation, the spatial variation of the Coriolis parameter has to be included, too. The present extension of PM70 also includes replacing the local time derivative by material derivative and using angular momentum as a dynamical variable instead of the zonal velocity. The latter approach was successfully employed to study inertial and

near-geostrophic flows (Paldor and Boss, 1992; Rom-Kedar *et al.,* 1997) and equator crossings (Dvorkin and Paldor, 1999). The method provided a simple and powerful tool that helps unravel the dynamics underlying the numerically computed solutions of the governing equations. Compared with Eulerian models (Böning and Cox, 1988; Figueroa and Olson, 1989) the resolution of Lagrangian models is unlimited so water columns can originate from any location and their trajectory followed to any desired distance. Thus, Lagrangian models allow the identification of regions in phase space where small changes in either an initial condition or a parameter value have a drastic effect on the resulting trajectory.

The inclusion of drag in the present model renders the dynamics dissipative in contrast to the Hamiltonian structure of the inertial, quasi-geostrophic and cross-equatorial cases. The system's fixed points (steady states) can thus be sinks and spirals so the inclusion of zonal- or time-variation of the wind stress can have a more dramatic effect on the drifter trajectories. A complete analysis of a dissipative nonlinear dynamical system cannot be accomplished in a single paper and the present study is only a first step in unraveling the intricacies associated with drifter trajectories.

Two points are now in order. First, the analyses of PM70 and the present model focus solely on the momentum equations, completely ignoring the continuity equation, so it cannot be applied straightforwardly to oceanic (fluid) flows. However, the fast horizontal dispersal shown in Figure 1 clearly demonstrates that continuity does not play a role in the dynamics of drifter trajectories in the ocean, so this study is as relevant to water flows as drifter trajectories. Second, in the title of this work "spherical earth" indicates that the analysis will be significantly altered if the centrifugal force associated with the rotation of perfect "sphere" is included. The following analysis is only valid when this centrifugal term can be neglected, as is the case when Earth's eccentricity of 0.003 (that balances the centrifugal term with the horizontal component of gravity) is taken into account.

2. The Ekman transport on the Earth

Consider the time derivatives (denoted by the subscript t) of the vertically averaged zonal (u) and meridional (v) velocity components of a water column in the bulk surface mixed layer (depth h) on the rotating (frequency Ω) Earth (radius R). Combining the effects of Earth's curvature with the slab parameterization of the wind stress the momentum equations (see Eqs. 4.12.14–15 and 9.3.6 in Gill, 1982 and PM70) are:

$$u_t = v \sin(\phi)\{2\Omega + u/(R\cos(\phi))\} + \Gamma^x/(h\rho) - \gamma^* u, \tag{1a}$$

in the zonal (λ) direction and,

$$v_t = -u \sin(\phi)\{2\Omega + u/(R\cos(\phi))\} + \Gamma^y/(h\rho) - \gamma^* v, \tag{1b}$$

in the meridional (ϕ) direction. The surface wind stress is $\Gamma \equiv (\Gamma^x, \Gamma^y)$, ρ is the density of water and derivatives on the l.h.s. are material derivatives and the transport in the layer is simply hu and hv.

The dissipation of kinetic energy is parameterized by $\gamma^* > 0$ (units: time^{-1}), where $1/\gamma^*$ measures the *e*-folding time for the velocity to approach zero once the wind ceases to blow. The *f*-plane, PM70 model predicted correctly the observed currents with a drag time, $1/\gamma^*$, of 2–8 days (Kundu, 1976; Käse and Olbers, 1979). The terms proportional to 2Ω in Eqs. (1a, b) are the Coriolis force and the $u/(R\cos(\phi))$ terms arise from the spherical geometry. The latter terms are usually neglected in *f*-plane studies since $u/(2\Omega R\cos(\phi))$ is of order 10^{-3} but in the present study they are retained so as to enable an exact evaluation of the changes in the angular momentum along the trajectory.

In addition to these equations the changes in the column's longitude (λ) and latitude (ϕ) are:

$$\lambda_t = u/(R\cos(\phi)), \tag{1c}$$

$$\phi_t = v/R. \tag{1d}$$

System (1) is naturally nondimensionalized using the length scale R and the time scale $(2\Omega)^{-1}$. For terrestrial values the velocity scale of $(2\Omega R)$ equals 930 m s^{-1} so the nondimensionalized speed of surface flow in the ocean is order 10^{-4}–10^{-3}. The nondimensional drag coefficient γ corresponding to a dimensional decay time of n days is simply $1/(4n\pi) \approx 0.08/n$.

The acceleration scale is $(2\Omega)^2 R \approx 0.135$ m s^{-2} so the nondimensional acceleration, τ, due to a vertically averaged wind stress of $\Gamma/(h\rho)$ is: $\tau = \Gamma/(\rho h 4\Omega^2 R)$. For $|\Gamma| =$ 0.2 N m^{-2} (10 m s^{-1} winds), Ekman layer thickness, h, of order 20 m and $\rho = 10^3$ kg m^{-3} τ is 10^{-4}. Aside from the $(4\Omega^2 R\rho)^{-1} = 1/135$ m^2 s^2 kg^{-1} factor, τ is proportional to Γ/h—the wind stress divided by the column's thickness—so its sign is determined by the wind direction. Assuming that τ only has a zonal component that varies with latitude, $\tau^x(\phi)$, the scaled version of system (1) becomes:

$$u_t = v\sin(\phi)\{1 + u/(\cos(\phi))\} + \tau^x(\phi) - \gamma u, \tag{2a}$$

$$v_t = -u\sin(\phi)\{1 + u/(\cos(\phi))\} - \gamma v, \tag{2b}$$

$$\lambda_t = u/\cos(\phi), \tag{2c}$$

$$\phi_t = v. \tag{2d}$$

In system (2) the effect of the Coriolis force (including the geometric terms) appears in a similar way in Eqs. (2a) and (2b). Replacing the zonal momentum equation, (2a), by an equation for the evolution of the angular momentum, which is affected by body forces only, facilitates the analysis since the Coriolis term appears, in a different form, only in the meridional momentum (2b). This change of variables where the zonal velocity, u, is replaced by the angular momentum was proven useful in analyses of similar systems (Rom-Kedar *et al.,* 1997; Dvorkin and Paldor, 1999). The nondimensional form of the angular momentum, D, is:

$$D = \cos(\phi)(\tfrac{1}{2}\cos(\phi) + u) \tag{3a}$$

so u can be expressed in terms of D as:

$$u = D/\cos(\phi) - \tfrac{1}{2}\cos(\phi). \tag{3b}$$

Substituting D for u in system (2) one gets:

$$\phi_t = v, \tag{4a}$$

$$v_t = \tfrac{1}{2}\sin(2\phi)\{\tfrac{1}{4} - D^2/\cos^4(\phi)\} - \gamma v, \tag{4b}$$

$$D_t = \tau^x\cos(\phi) - \gamma(D - \tfrac{1}{2}\cos^2(\phi)), \tag{4c}$$

$$\lambda_t = D/\cos^2(\phi) - \tfrac{1}{2}. \tag{4d}$$

The calculation of the longitude time series, $\lambda(t)$, in Eq. (4d) is required only for calculating the geographic trajectory $(\lambda(t), \phi(t))$ but has no effect on the dynamics, which is determined by system (4a–c) only. Thus, $\lambda(t = 0) = 0$ is assumed, without loss of generality, in the rest of this work.

It should be noted that since u is of order 10^{-3}, the value of D (Eq. 3a) is very nearly $\frac{1}{2}\cos^2(\phi)$ i.e. close to $\frac{1}{2}$ at low latitudes and even in midlatitudes ($\phi \approx 45°$) the value of D is near 0.25. The value of D approaches 0.0 only near the poles, $\phi \approx \pm 90°$.

System (4) is analyzed in the next section while in Section 4 it is integrated numerically.

3. Analytical considerations

A natural starting point for analyzing the nonlinear system (4) is the inertial case when all body forces vanish. The dynamics of this case were studied in detail in Paldor and Boss (1992) and Rom-Kedar *et al.* (1997) and the main results pertinent to model (4) are briefly summarized next.

a. The inertial flow

Setting both $\tau^x(\phi)$ and γ in the system (4) equal to zero Eq. (4c) implies that D is conserved so it becomes a model parameter instead of a system's variable. The dynamics is described by:

$$\phi_t = v, \tag{5a}$$

$$v_t = \tfrac{1}{2}\sin(2\phi)\{\tfrac{1}{4} - D^2/(\cos^4(\phi))\}, \tag{5b}$$

that conserves the kinetic energy $E_k = (v^2 + u^2)/2$ as no body forces are present. The conserved kinetic energy, E_k, provides a guess for the Hamiltonian of the system and, in terms of (v, ϕ) variables, it only requires that D be substituted for u using relation (3b) i.e.:

$$H = \tfrac{1}{2}[v^2 + (D/\cos(\phi) - \tfrac{1}{2}\cos(\phi))^2]. \tag{6}$$

It is easy to show that v and ϕ are indeed conjugate variables satisfying:

$$\phi_t = H_v \quad \text{and} \quad v_t = -H_\phi.$$

Thus, the set (5) comprises an integrable, 1-Degree-Of-Freedom (1-DOF) system and its dynamics is completely determined by the values of D and the Hamiltonian, H. System (5) has a pitchfork bifurcation at $D = 1/2$: For $D > 1/2$ there exists only one, elliptic, fixed point at the origin $(v_s, \phi_s) = (0, 0)$ while for $D < 1/2$ this fixed point at the origin turns hyperbolic and two elliptic fixed points arise at $(v_s, \phi_s) = (0, \pm\arccos([2|D|]^{1/2}))$. The evolution of the inertial system is completely determined by the initial conditions (v_0, ϕ_0) and the value of the parameter D (determined by ϕ_0 and u_0).

The motion near the elliptic points ($v_s = 0$; $\phi_s = 0$, $D > 1/2$ and $\phi_s = \pm\arccos((2|D|)^{1/2})$, $D < 1/2$) consists of inertial oscillations, i.e. zonally migrating (v, ϕ) circles. The oscillations' periods are given by the imaginary eigenvalues of the matrix that obtains from linearizing system (5) near the fixed points. The result is that the eigenvalues are the roots of the quadratic equations:

$$\mu^2 = (1/4 - D^2), \quad \text{when} \quad D > 1/2 \tag{7a}$$

$$\mu^2 = -\sin^2(\phi_s) = 2D - 1, \quad \text{when} \quad D < 1/2\,. \tag{7b}$$

The eigenvalues in Eq. 7b are imaginary so the trajectory of a water column launched with $v_0 = 0$ from a latitude ϕ_0 close to (but not equal) $\phi_s \equiv \arccos([2|D|]^{1/2})$ will consist of pure (anticyclonic) oscillations in (v, ϕ) with a frequency equal to $\sin(\phi_s)$. Thus, if $\phi(t = 0) = \phi_0$ is higher (lower) than ϕ_s it will move initially equatorward (poleward) so initially the latitude, $\phi(t)$, will decrease (increase).

b. The drag-free case

When $\tau^x(\phi) \neq 0$ is assumed in Eqs. (4a–c), (but γ is still set equal to zero) one gets:

$$\phi_t = v, \tag{8a}$$

$$v_t = 1/2 \sin(2\phi)\{1/4 - D^2/\cos^4(\phi)\}, \tag{8b}$$

$$D_t = \tau^x(\phi) \cos(\phi). \tag{8c}$$

System (8) differs fundamentally from the inertial system (5). Kinetic energy changes with time since work is being continuously done on the moving column by the wind stress, so for general wind stress, when no potential exists (but a particular counter example is given below), the system is not Hamiltonian. As a result, the zonal velocity, u, is unbounded and so is D and at sufficiently long times Eq. (8c) implies that the sign of D (and u) equals that of $\tau^x(\phi)$.

From Eq. (8c) one can immediately conclude that the latitudes of the system's fixed points, ϕ_s, all satisfy $\tau^x(\phi_s) = 0$ and Eqs. (8a, b) imply that any fixed point (v_s, ϕ_s, D_s) has to satisfy:

$$(v_s, \phi_s, D_s) = (0, \phi_s, \tfrac{1}{2}\cos^2(\phi_s)).$$

Since ϕ_s are the latitudes of vanishing wind stress the number of fixed points is determined by the meridional form of zonal wind stress. The value of D at the fixed points $D_s = \frac{1}{2}\cos^2(\phi_s) < \frac{1}{2}$ suggests that these are the counterparts of the elliptic fixed points of the inertial system (5) in the $D < \frac{1}{2}$ case. The type of the fixed points is determined by the eigenvalues of the (3 by 3) matrix obtained by linearizing system (8) near these points. A negative (positive) eigenvalue indicates that near the fixed point there is a direction in (v, ϕ, D) space along which the system is attracted-to (repelled-from) the fixed point, respectively (this direction is determined by the corresponding eigenvector). Imaginary eigenvalues imply oscillations (e.g. inertial) about the fixed point, i.e. circles in phase space, while complex ones combine the two types of time dependence i.e., spirals and sinks.

When system (8) is linearized about a fixed point the three eigenvalues, denoted as μ_i, $i = 1 \ldots 3$, are determined by the roots of the characteristic polynomial

$$\eta^3 + \eta + \tau_\phi(\phi_s)/\sin^2(\phi_s) = 0, \quad \phi_s \neq 0 \tag{9}$$

where $\eta \equiv \mu/\sin(\phi_s)$ and $\tau_\phi(\phi_s)$ denotes the ϕ-derivative of the wind stress evaluated at $\phi = \phi_s$. The case $\phi_s = 0$ (vanishing wind stress on the equator) is degenerate as all three eigenvalues, $\mu_i = 0$, $i = 1 \ldots 3$ equal zero so 2nd order terms are required. Regardless of the value/sign of $\tau_\phi(\phi_s)/\sin^2(\phi_s)$ for $\phi_s \neq 0$ one root of Eq. (9) is always real and the other two constitute a complex conjugate pair.

The eigenvalue equation (9) is interpreted in two steps. First, the homogeneous equation is analyzed followed by an analysis of the changes due to the inclusion of the inhomogeneous term.

i. The case when ϕ_s is a multiple zero of $\tau^x(\phi)$ [i.e. $\tau_\phi(\phi_s) = 0$]. When $\tau_\phi(\phi_s)$ vanishes the real root of Eq. (9), $\eta^3 + \eta = 0$, vanishes too, $\mu_1 = 0 = \eta_1$, while the other two are purely imaginary, $\eta^2 = -1$, i.e. $\mu_{2,3} = \pm\sin(\phi_s)(-1)^{1/2}$. Thus, the system evolves near ϕ_s, in an identical way to the inertial system (5): Along one direction (the eigenvector belonging to μ_1) the system remains constant (to first order) in time, as it does along the D direction in the inertial case. In the perpendicular plane, spanned by the eigenvectors belonging to μ_2 and μ_3, the system merely oscillates with frequency $\sin(\phi_s)$ identical to the frequency of the inertial oscillations in the (v, ϕ) plane near its elliptic fixed points—Eq. (7b). This suggests that the real root of (9), $\mu_1 = 0$ corresponds to the D coordinate while the complex pair, $\mu_{2,3}$ corresponds to the (v, ϕ) plane. A calculation of the (v, ϕ, D) eigenvectors confirms this inference.

It can be concluded from this analysis that to first order in time and in the vicinity of latitudes where both the wind forcing and its ϕ-derivative vanish, the trajectory oscillates as in the inertial case. For longer times, these oscillations are compounded by the slow temporal changes in D as determined by Eq. (8c) so the realization of these oscillation at

intermediate times rests upon the changes in D being commensurate with those in ϕ. Consider, for example, a northward initial displacement from the fixed point: $\phi_0 > \phi_s$. In this case the inertial motion requires that ϕ decreases at first which, for small enough u, is accomplished by an increase in the value of D. According to Eq. (8c) this initial increase in D due to the inertial motion agrees with the direct changes in D only when $\tau^x(\phi_0)$ is positive. On the other hand, if $\tau^x(\phi_0)$ is negative ($\tau^x(\phi)$ has a maximum at ϕ_s) then D **decreases** initially (Eq. 8c) which contradicts the tendency of the inertial oscillations. Similar considerations apply to the case when $\phi_0 < \phi_s$.

ii. The case when ϕ_s is a simple zero of $\tau^x(\phi)$ [i.e. $\tau_\phi(\phi_s) \neq 0$]. In this case, the real eigenvalue is determined by the intersection of the real cubic $f(\eta) \equiv \eta^3 + \eta$ with the horizontal line $g(\eta) \equiv -\tau_\phi(\phi_s)/\sin^2(\phi_s)$. Thus, $\tau_\phi(\phi_s) \neq 0$ causes the real eigenvalue, $\mu_1 = 0$, of the $\tau_\phi(\phi_s) = 0$ case to be shifted in accordance with the sign of $\tau_\phi(\phi_s)$. Since $f(\eta)$ is monotonically increasing with η for all $\eta(f_\eta(\eta) \equiv 1 + 3\eta^2 > 0)$ and since sign $(g(\eta)) = -\text{sign}\,(\tau_\phi(\phi_s))$, when $\tau_\phi(\phi_s) > 0$, μ_1 is shifted downward—$\mu_1 < 0$—while when $\tau_\phi(\phi_s) < 0 - \mu_1 > 0$ i.e. sign $(\mu_1) = -\text{sign}\,(\tau_\phi(\phi_s))$.

The three eigenvalues given by the roots of Eq. (9) satisfy $\mu_1 + \mu_2 + \mu_3 = 0$ (i.e. the negative of the coefficient of the quadratic term). Thus, the real part of the complex conjugate pair satisfies $Re\{\mu_{2,3}\} = -\frac{1}{2}\mu_1$ so $Re\{\mu_{2,3}\} = \text{sign}\,(\tau_\phi(\phi_s))$ i.e., the nonoscillatory evolution results from the nonzero wind stress' curl at ϕ_s. For small initial departure the system spirals away from the fixed point in the (v, ϕ) plane when $\tau_\phi(\phi_s) > 0$ and along D when $\tau_\phi(\phi_s) < 0$. Since at least one of the three eigenvalues has a positive real part *all steady states are unstable* as long as $\tau_\phi(\phi_s) \neq 0$!

iii. A Hamiltonian dynamics with nonvanishing wind forcing. The particular case when the wind forcing satisfies: $\tau^x(\phi)\cos(\phi) = \text{Const.}\ (\equiv A)$ is peculiar because the system is Hamiltonian despite the work done by the wind forcing. The interpretation of $\tau^x(\phi)\cos(\phi) = \text{Const.}$ is that upon completing a revolution around the globe along a latitude circle (of length $2\pi\cos(\phi)$) the change in the water column's zonal velocity is independent of the latitude. Eq. (8c) implies that in this case no steady states (i.e. fixed points) exist since D_t never vanishes. In (v, ϕ) plane, however, the origin is a fixed point (stable for $D^2 > \frac{1}{4}$ and unstable for $D^2 < \frac{1}{4}$) so the final latitude of the water column is the equator with zero meridional velocity while the zonal velocity and the longitude increase or decrease indefinitely. Simply, the water column is accelerated by the wind forcing (eastward or westward depending on the sign of A) so its zonal speed is ever increasing and, since the Coriolis force vanishes there, the equatorial zonal flow is not compounded by inertial oscillations. From an analytic viewpoint, a potential can be defined in this case so that a total energy that is conserved along the trajectory can be defined and the system can be shown to be Hamiltonian. In analogy with the inertial case, Eq. (6), we define the Hamiltonian as:

$$H = \tfrac{1}{2}\left[v^2 + (D/\cos(\phi) - \tfrac{1}{2}\cos(\phi))^2\right] - A\lambda. \tag{10}$$

Since the potential energy, $E_p \equiv -A\lambda$ (the negative sign implies that the potential energy decreases with increasing longitude which enables the increase in kinetic energy) does not depend on v or ϕ these variables remain conjugate, as in the inertial case, while a direct inspection of Eqs. (8c), (4d) shows that D and λ now constitute an additional pair of conjugate variables satisfying:

$$\lambda_t = H_D \quad \text{and} \quad D_t = -H_\lambda.$$

The conservation of total energy, i.e. the Hamiltonian Eq. (10), provides a constraint that has to be satisfied by any numerical solution of system (8 and 4d). The system is now 2-DOF and even a small perturbation (e.g. time- or zonal-dependence of the wind forcing) will significantly alter the trajectory of a given water column and the statistical characteristics of an ensemble of drifters.

Since D_t is constant ($\equiv A$) $D(t) = D_0 + At$ so when D passes the bifurcation value of ½ (i.e. ϕ near 0) the longitude evolution is approximated by $\lambda(t) \approx \frac{1}{2} At^2$. These estimates provide further checks (in addition to the conservation of the Hamiltonian) on the numerical calculations.

c. The effect of drag

The inclusion of drag ($\gamma \neq 0$ in Eqs. 4b, c) entails two changes in the analysis of Subsection *b*.

First, the system now possesses a new fixed point $(v_s, \phi_s, D_s) = (0, 0, \tau^x(0)/\gamma + \frac{1}{2})$ where the zonal velocity, given by $u_s = \tau^x(0)/\gamma$, does not vanish. At this fixed point the energy production due to the work done by the wind stress on the moving column, $\tau^x(0)u$, is balanced by the dissipation of kinetic energy, $(2\gamma)\,\frac{1}{2}\,u^2$. The longitude of the column, $\lambda(t)$, changes with time at a constant rate given by Eq. (4d): $\lambda_t = u_s = \tau^x(0)/\gamma$.

The eigenvalues of the linearized system, μ_i, $i = 1 \ldots 3$, near this new fixed point satisfy:

$$\mu(\mu + \gamma)^2 - (\tfrac{1}{4} - D_s^2)(\mu + \gamma) = 0. \tag{11}$$

Thus, there always exists one real negative root, $\mu_1 = -\gamma$, and the remaining two roots are given by $\mu_{2,3} = (-\gamma \pm [\gamma^2 + 4(\frac{1}{4} - D_s^2)]^{1/2})/2$. For $(\frac{1}{4} - D_s^2) \equiv -u_s(1 + u_s) > 0$ one of the two roots is real positive and the fixed point is unstable. On the other hand, for $(\frac{1}{4} - D_s^2) < 0$ (i.e. $u_s > 0$ and the unphysical case, $u_s < -1$) both eigenvalues have negative real parts so the fixed point is stable. Thus, westerly winds ($\tau^x(0) > 0$) and unphysically strong easterlies ($\tau^x(0) < -\gamma$) are both associated with a stable steady state while for physically acceptable easterly winds any deviation from the steady state will grow exponentially with time.

Second, in addition to this new fixed point all the fixed points calculated in Subsection *b* for the $\gamma = 0$ case still prevail when γ is nonzero since both v_s and u_s vanish ($D_s = \frac{1}{2}\cos^2(\phi_s)$) there so the Rayleigh drag terms vanish there even when $\gamma \neq 0$. However,

the stability characteristic of the points changes drastically when γ does not vanish. The characteristic equation (9) becomes:

$$\eta[(\eta + \alpha)^2 + 1] + \tau_\phi(\phi_s)/\sin^2(\phi_s) = 0, \qquad \phi_s \neq 0, \tag{12}$$

where $\alpha \equiv \gamma/\sin(\phi_s)$ and η is related to the eigenvalue, μ, by $\eta = \mu/\sin(\phi_s)$. Thus, in this case, the cubic equation contains a quadratic term with a real coefficient 2α so the sum of its three roots is $\eta_1 + \eta_2 + \eta_3 = -2\alpha$ and the three eigenvalues, $\mu_{1,2,3}$, add up to the real *negative* number (-2γ). Thus, all three eigenvalues *can* have negative real parts so that the inherent instability of the $\gamma = 0$ case, where at least one eigenvalue has a positive real part, is removed by the drag force.

The analysis of Eq. (12) can be carried out in similar manner to the drag-free case; First the case when the inhomogeneous term, $\tau_\phi(\phi_s)/\sin^2(\phi_s)$, vanishes is analyzed, followed by an analysis of the changes when this term is not zero. In the homogeneous case, Eq. (12) has a zero root ($\eta_1 = 0 = \mu_1$) while the other two roots are the roots of the quadratic equation:

$$(\eta + \alpha)^2 + 1 = 0,$$

i.e. $\eta_{2,3} = -\alpha \pm (-1)^{1/2}$ or $\mu_{2,3} = -\gamma \pm (-1)^{1/2} \sin(\phi_s)$. Since, by definition, γ is real positive, the effect of drag is, as expected, to turn the neutral fixed points of the inertial oscillations into stable spirals.

The effect of nonzero wind forcing gradient, $\tau_\phi(\phi_s) \neq 0$, in Eq. (12) is similar to that in the drag-free case. The real root of the homogeneous Eq. (12), η_1, (i.e. the zero root of the $\tau_\phi(\phi_s) = 0$ case) is now determined by the intersection of the parabola $f(\eta) \equiv (\eta + \alpha)^2 + 1$ with the hyperbola B/η ($B \equiv -\tau_\phi(\phi_s)/\sin^2(\phi_s)$) both shown in Figure 2 for several values of B. It is easy to show that sign (η_1) = sign (B) = $-$sign $(\tau_\phi(\phi_s))$ as in the drag-free case. Since the sum of the three roots equals (-2α) regardless of the value of $\tau_\phi(\phi_s)$, the real part of the pair of complex conjugate roots has to satisfy $Re\ \{\eta_{2,3}\} = -\alpha - \frac{1}{2}\eta_1$ which is negative provided $\eta_1 > -2\alpha$.

In order for the fixed point at ϕ_s to be stable the real part of all three eigenvalues has to be negative which occurs for $0 > \eta_1 > -2\alpha$. From the graph of $f(\eta)$ shown in Figure 2 it is evident that for η in the range $(-2\alpha, 0)$ this parabola satisfies $f(\eta) < (1 + \alpha^2)$. Thus, in order for B/η to intersect $f(\eta)$ at some $0 > \eta > -2\alpha$, B has to satisfy: $-2\alpha(1 + \alpha^2) < B < 0$ which, in terms of the forcing gradient, implies that stability is guaranteed only for:

$$0 < \tau_\phi(\phi_s) < 2\gamma \sin(\phi_s)(1 + \gamma^2/\sin^2(\phi_s)).$$

In reality, since the nondimensional value of $\tau^x(\phi) \approx 10^{-4}$ is three orders of magnitude smaller than $\gamma \approx 10^{-1}$, this stability condition holds everywhere for sufficiently smooth $\tau^x(\phi)$ provided $\phi_s \neq 0$.

Finally, the rate of change of kinetic energy, $E_k \equiv \frac{1}{2}(u^2 + v^2)$, can be calculated at any time and for any location in phase space by multiplying Eq. (2a) by u and Eq. (2b) by v. Adding the resulting equations and rearranging, one gets $(E_k)_t = \tau^x u - 2\gamma E_k$ so the

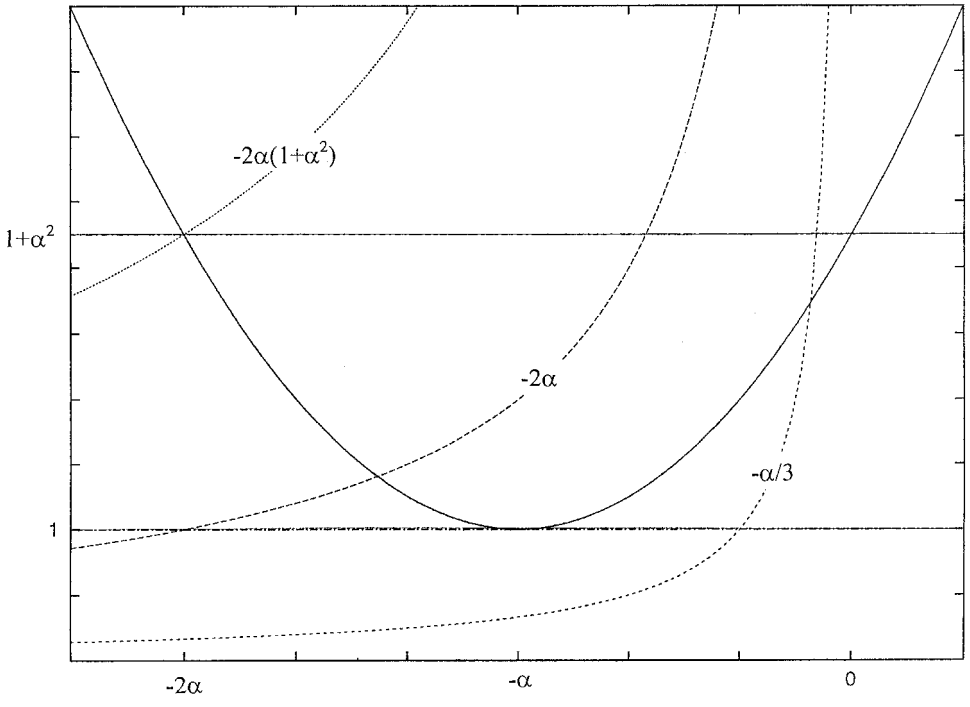

Figure 2. The determination of the stability of the fixed point at ϕ_s, the latitude of vanishing wind forcing, when drag is included. The real eigenvalue of the D direction, η_1, is determined by the intersection of the parabola $f(\eta) = 1 + (\alpha + \eta)^2$ (solid curve) with the hyperbola B/η (shown for three negative values of B marked on the corresponding dashed curves). For $B > 0$ the eigenvalue η_1 is positive (B/η intersects $f(\eta)$ only at $\eta > 0$) while for $B < 0$, $\eta_1 < 0$. The real part of the other two eigenvalues, Real$\{\eta_{2,3}\}$ equals $(-\alpha - \frac{1}{2} \cdot \eta_1)$ so it is negative only for $\eta_1 > -2\alpha$. All three eigenvalues have negative real parts only if η_1 is within the range $-2\alpha < \eta_1 < 0$ which implies that $1 < f(\eta) < (1 + \alpha^2)$ (these bounds are marked by the two horizontal lines). For B/η to intersect $f(\eta)$ in the range $-2\alpha < \eta < 0$, the value of B has to satisfy: $-2\alpha \cdot (1 + \alpha^2) < B < 0$.

drag's effect is simply to restore any deviation of the kinetic energy from its steady value, $E_{ks} \equiv \tau^x u/(2\gamma)$ (with $\tau^x u$ taken as independent of E_k), back to this value. The relaxation of the kinetic energy to this steady value is exponential with an e-folding time of $(2\gamma)^{-1}$.

These analytical results help interpret, and validate, the numerical solution of system (4) for different parameter values and initial conditions.

4. Model trajectories

System (4) was integrated numerically using a 5^{th} order Runge-Kutta scheme with a 10^{-7} tolerance between $t = 0$ and $t = T_f$ where the final time, T_f, is less than 40π; i.e., 10 days. In each case the calculated geophysical trajectories, $(\lambda(t), \phi(t))$, of a water column

are shown (top panel) in addition to phase space, (v, ϕ), diagrams (middle panel) and a graph of $D(t)$ (bottom panel). The latter diagrams illustrate the analytical point being interpreted/validated and the former simulates the corresponding trajectory of the water column as observed by tracking a drogued drifter. The beginning and end of the trajectory are marked by "x" and "o," respectively.

The meridional shape of the wind forcing, $\tau^x(\phi)$, the launching latitude, ϕ_0, and the value γ are all varied in order to cover a broad spectrum of scenarios while the initial values of v, λ and D were set, to 0, 0 and $\frac{1}{2}\cos^2(\phi_0)$, respectively. The generic form of the wind forcing in all cases (the order follows that of Section 3) is:

$$\tau^x(\phi) = \tau_0 \sin^n(k(\phi - \phi_{ce})), \tag{13}$$

where k, taken to equal 2, is the wavenumber and ϕ_{ce} is the central latitude of the wind forcing (which vanishes at all latitudes, ϕ_s, satisfying: $-\pi/2 < \phi_s = \phi_{ce} \pm m\pi/k < \pi/2$ for some integer m). The multiple zero case, $\tau_\phi(\phi_s) = 0$, obtains for $n > 1$ while $n = 1$ yields the simple zero, $\tau_\phi(\phi_s) \neq 0$. The amplitude, τ_0, was varied so as to yield wind forcing, $\tau^x(\phi)$, not much larger than 10^{-4} (see Section 2) throughout the entire travel time (and latitude range) of the water column.

a. Drag-free simulations

Recall from Section 3 that ϕ_s, the latitudes of vanishing wind stress, are the fixed points.

i. The behavior near the elliptic fixed point when ϕ_s is a multiple zero of $\tau^x(\phi)$ [$\tau_\phi(\phi_s) = 0$]. The wind forcing parameters that demonstrate the inertial oscillations of Subsubsection 3b(i) are:

$$n = 2,\ k = 2,\ \phi_{ce} = 0.3\ (\approx 17.189\text{N}) \quad \text{and} \quad \tau_0 = 0.15. \tag{14}$$

The central latitude, 17.189N, is one of the fixed points of the system because D_t vanishes there and by our choice of $n = 2$ the wind forcing is directed everywhere eastward so at ϕ_{ce} it has a local minimum. Therefore, from the discussion in Section 3b, at short times we expect D to increase, and hence the latitude to decrease. This change in D agrees with the direct change of ϕ anticipated by the inertial oscillations when the initial latitude ϕ_0 is higher than ϕ_{ce} and opposes it when $\phi_0 < \phi_{ce}$. The results shown in Figure 3 for the case ϕ_0 $(=0.31) > \phi_{ce}$ $(=0.3)$ demonstrate these findings: The inertial oscillations are evident in the (v, ϕ) plane plot as the equatorward (left) migrating, nearly closed, loops. The values of both v and λ remain negligibly small, and those of ϕ and D deviate only slightly from the initial ones, throughout the entire integration interval of $t = (0, 50)$ i.e. about four days. The subsequent small drift in D which causes a further, slower, general decrease in ϕ can be seen clearly in the geographic, (λ, ϕ), trajectory but even with this latitude drift the trajectory remains north of the fixed point ($\phi_s \equiv \phi_{ce} = 17.189°$) even at $t = 50$. The changes in D are very small (and monotonic) during the entire

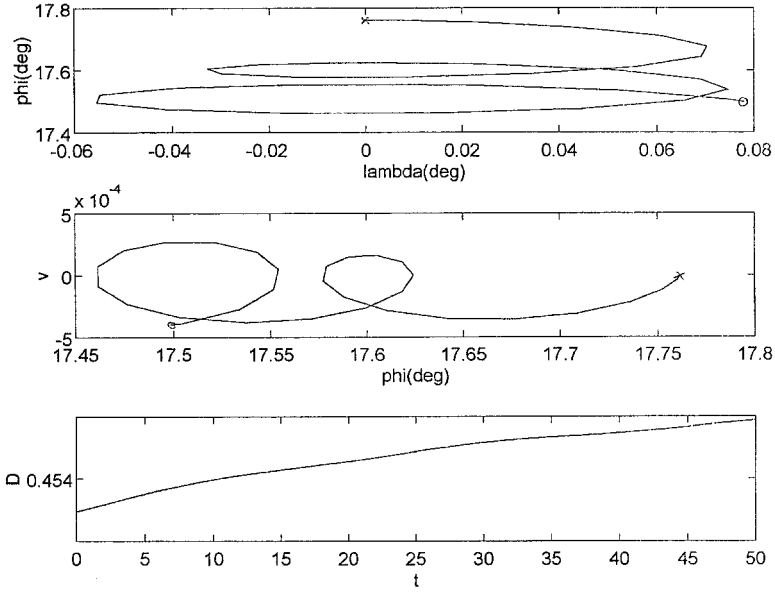

Figure 3. The geographic trajectory (top panel), phase plane portrait (middle panel) and changes in angular momentum (bottom panel) in the drag-free case ($\gamma = 0$) near the latitude $\phi_{ce} = 0.3$ where both the wind forcing and its meridional-gradient vanish. The initial latitude is 0.31 (0.01 Rad. north of ϕ_{ce}) so for small zonal velocity the direct changes in D are in accordance with the change of latitude by inertial flow. Wind forcing is given by Eq. (13) with $k = 2$, and $\tau_0 = 0.15$. Initial and final points are marked by x and o, respectively.

integration time as both latitude and kinetic energy of the water column (estimated by the maximal value of v) have not changed much.

In contrast to this, in Figure 4 the integration was done for identical model parameters but with the initial latitude set to $\phi_0 = 0.29$ i.e. 0.01 Rad. (about half a degree of latitude) *south* of the fixed point's latitude $\phi_s = \phi_{ce} = 0.3$. In this case, initially, the changes in ϕ due to the changes in D are in the opposite sense to the direct changes in ϕ due to the inertial oscillations. This causes significant differences between this and the former cases: No inertial oscillations are encountered in either the (v, ϕ) portrait or the geographic, (λ, ϕ), trajectory and the latitude changes are much faster—at $t = 50$ the trajectory is located about 8° south of the fixed point at 17.189N. Also, the changes in D are $O(1)$ so D reaches a value very close to 0.5, where the dynamics is not at all affected by the existence of a fixed point at $\phi_s = 0.3$. When the sign of τ_0 is reversed the large changes occur when ϕ_0 is slightly above the fixed point (not shown). This supports the conclusion that trajectory is very strongly affected by whether or not the direct, wind-forced, changes in D are commensurate with the changes in ϕ due to inertial oscillations.

ii. The behavior near the Elliptic fixed point when ϕ_s *is a simple zero of* $\tau^x(\phi)[\tau_\phi(\phi_s) \neq 0]$. The wind profile assumed for demonstrating the main flow features in this case (considered

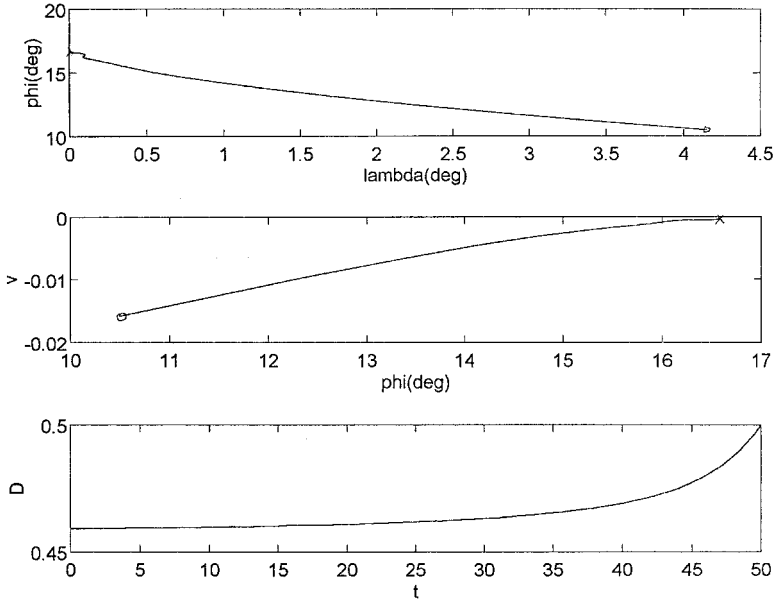

Figure 4. Same as Figure 3 but the initial latitude is 0.29 (0.01 Rad. south of ϕ_{ce}) so the explicit changes in D do not permit the inertial oscillations to take place.

analytically in Subsubsection 3b(ii)) has the form given by Eq. (13) with the parameters:

$$n = 1;\ k = 2;\ \phi_{ce} = 0.3\ (\approx 17.189\text{N}) \quad \text{and} \quad \tau_0 = 0.01. \tag{15}$$

The amplitude, τ_0, was decreased in this case to 0.01 so as to ensure that the magnitude of $\tau^x(\phi)$ is similar to that of the previous subsection throughout the entire trajectory. Unlike the previous case, for $n = 1$ the wind forcing changes sign at $\phi = \phi_{ce}$. The real part of all eigenvalues does not vanish, which implies that spirals replace the (midlatitude, inertial) centers encountered in the previous case. The results of the integrations shown in Figure 5 demonstrate these findings. No significant difference is evident when the integration starts from a latitude higher than ϕ_{ce} (Fig. 5a) or lower than ϕ_{ce} (Fig. 5b) and the overall change in the values of v, ϕ, D and λ throughout the entire integration time of $t = (0, 50)$ is similar in both cases. This is an immediate consequence of the inherent instability that exists for any $\tau^x(\phi)$ predicted in Subsubsection 3b(ii). In addition, these changes are much smaller than those of Figure 4 despite the larger wind forcing used here in the immediate vicinity of ϕ_{ce} (however, at latitudes more than 2° away from ϕ_{ce} the wind stress here is already smaller!) as compared with the $n = 2$ case.

iii. The Hamiltonian case. The case $\tau^x(\phi) = A/\cos(\phi)$, discussed in Subsubsection 3b(iii), provides an important particular case where the total energy, described by the Hamiltonian in Eq. (10), is conserved. This distribution of winds only approximates the

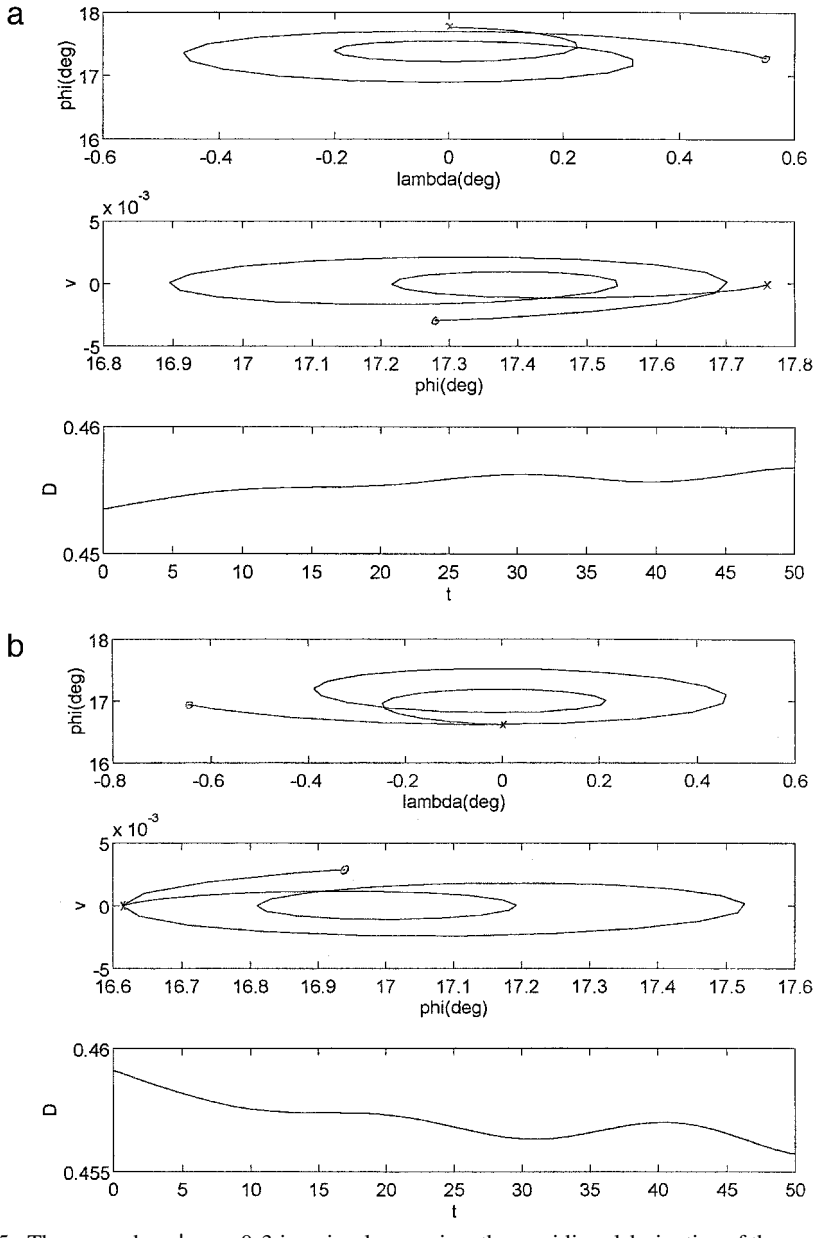

Figure 5. The case when $\phi_{ce} = 0.3$ is a simple zero; i.e., the meridional derivative of the zonal wind does not vanish there. The wind forcing amplitude is chosen to be $\tau_0 = 0.01$ so that the order of magnitude of the wind forcing along the trajectory is the same as that in Figure 4. Regardless of whether the initial displacement is northward, (a): $\phi_0 = 0.31$, or southward (b): $\phi_0 = 0.29$ the explicit changes in D by the wind forcing permit the inertial oscillations to take place.

situation in middle and low latitudes when the wind stress increases poleward. By contrast, right at the poles no zonal wind forcing exists so, by continuity, the wind forcing should diminish at high latitudes.

The numerical integration (not shown) demonstrate that even at $t = 40\pi$ the total energy is conserved (to $O(10^{-4})$ and that the angular momentum increases linearly, $D_t = A$, as expected.

b. Simulations with drag

When drag is included, a new steady state appears on the equator which is addressed first.

i. The behavior near the equatorial fixed point. The results of Subsection 3c point to the crucial effect that the relative values of γ and $\tau^x(0)$ have on the stability of this fixed point. In Figure 6 both the existence of the new fixed point right at the equator and the change in its stability when $\tau^x(0)$ is varied are demonstrated for $\gamma = 0.1$. The wind forcing parameters in Eq. (13) are:

$$n = 1; \qquad k = 2; \qquad \phi_{ce} = -0.3 \quad \text{and} \quad \tau_0 = 0.03, -0.4 \quad \text{and} \quad -0.03 \tag{16}$$

for the three cases considered in the first part of Subsection 3c. The central latitude, $\phi_{ce} = -0.3$, is shifted to the Southern Hemisphere to ensure that a water column originating at $\phi_0 = +0.4$ (22.9N) experiences a wind forcing of one sign throughout its entire equatorward motion and does not encounter one of the fixed points associated with vanishing wind stress.

The case $\tau_0 = 0.03$, where $\tau^x(0) = 0.017 > 0$, is shown in Figure 6a and it confirms the analytic expectation of a stable point for positive wind forcing at the equator. The same occurs for $\tau_0 = -0.4$ (i.e. $\tau^x(0) = -0.226 < -0.1 = -\gamma$) shown in Figure 6b. In contrast, the case $\tau_0 = -0.03$ shown in Figure 6c implies that $0 > \tau^x(0) = -0.017 > -0.1 = -\gamma$ and the instability in this case repels trajectory poleward. The final values of D in the stable cases shown in Figures 6a–b, 0.67 and -1.76, are in excellent agreement with the analytical estimate, $D_s = \frac{1}{2} + \tau^x(0)/\gamma$. In the unstable case shown in Figure 6c, the trajectory is repelled by the instability of the equator to such high latitudes that the value of D has to be close to zero so the steady state value of 0.33 is never realized.

Two additional points are apparent in the simulations shown in Figure 6. The first is that in the stable case shown in Figure 6b the u-velocity associated with $D \approx -2$ is unphysically large. This is a direct result of the unrealistically large wind forcing $\tau^x(0) = -0.4$ used here to demonstrate the stability of high westward-directed wind stress. The second point is that in the two stable cases (Figs. 6a and 6b) the initial rate of change in D (i.e. the slope of the $D(t)$ curve for $t < 1$, $D \approx D_0$) is very well approximated by its analytical estimate $-\gamma(D_0 - D_s)$. This estimate arises directly from the validity of the linear eigenvalue theory $\mu_1 \equiv D_t/D = -\gamma$ near the fixed point, $D = D_s$. By contrast, in the unstable case shown in Figure 6c the fixed point ($D_s = 0.33$) is never reached by the

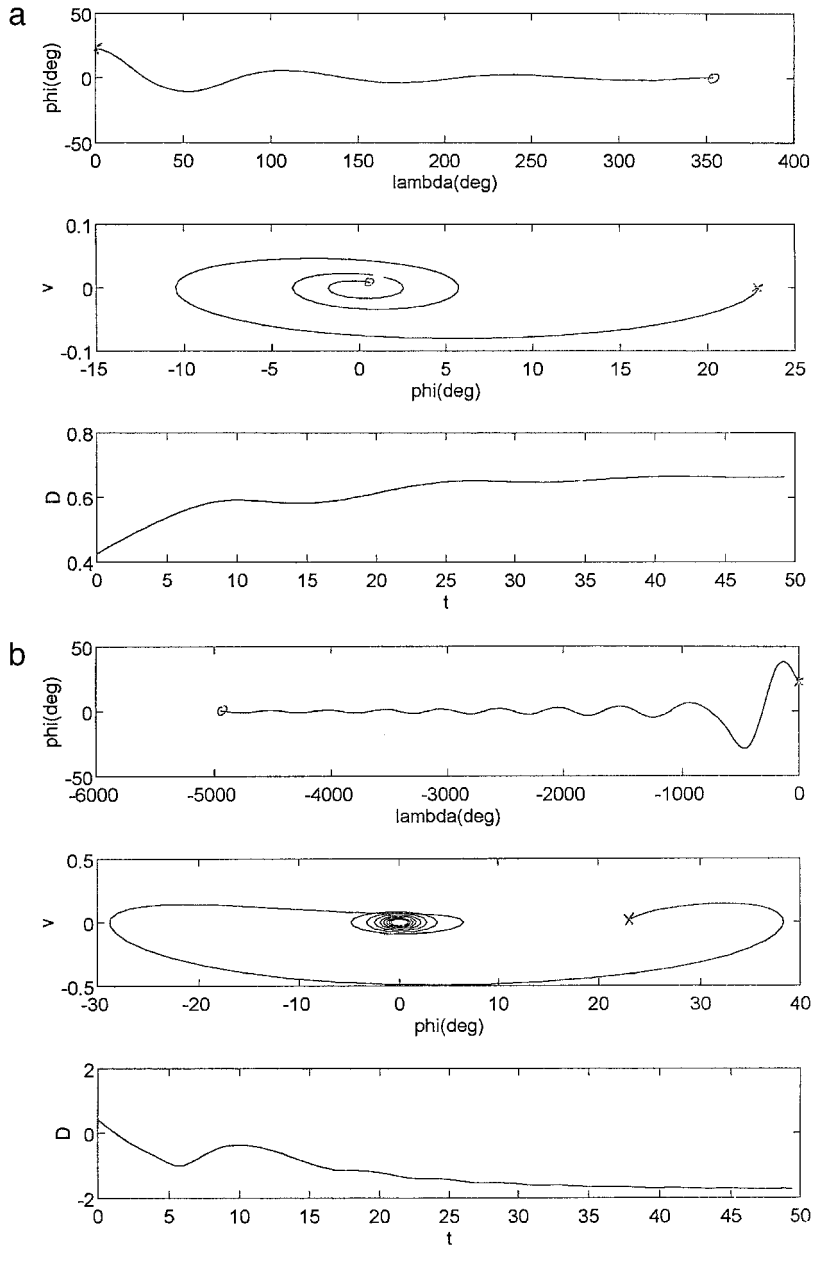

Figure 6. The effect of water drag on the trajectory near the equator for a drag coefficient, γ, equal to 0.1. The fixed point at the equator is attractive when the wind forcing there is positive, (a), or when it is sufficiently large and negative, (b). By contrast, when the wind forcing at the equator is weak and negative the equator is repulsive (c). The initial latitude is 0.4 in all cases. The wind forcing has the same latitude dependence as in Figure 5 (meridional wavenumber 2) but its zero is located in the Southern Hemisphere, at $\phi_{ce} = -0.3$ and its amplitude is: $\tau_0 = 0.03$ (a); $\tau_0 = -0.4$ (b); and $\tau_0 = -0.03$ (c).

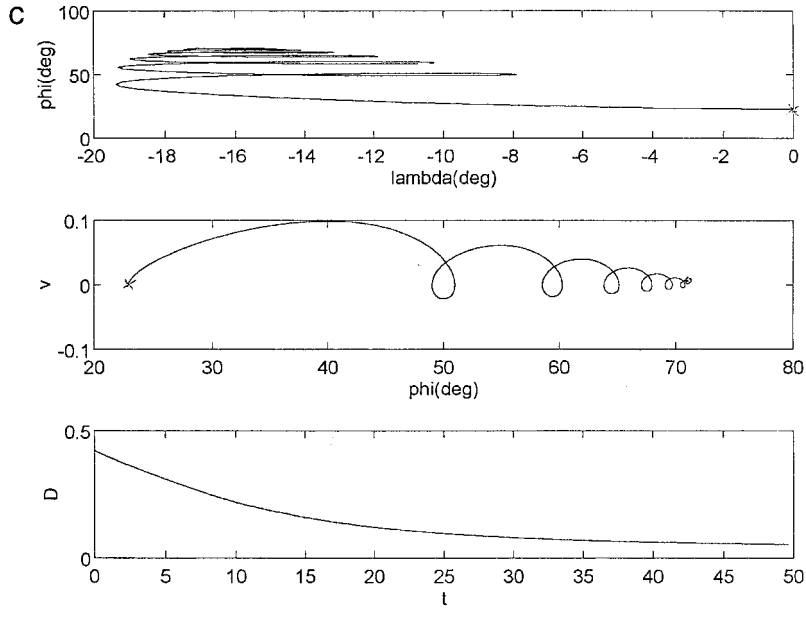

Figure 6.—*Continued*

trajectory and this is consistent with the initial rate of change in D (about -0.025 from the slope of the $D(t)$ curve shown in the lower panel of Fig. 6c) being nearly three times the analytical value: $-\gamma(D_0 - D_s) \approx -0.009$.

ii. The behavior near the fixed points of the drag-free system. A simple case where the inclusion of drag turns the neutral circles of the drag-free case into stable spirals is shown in Figure 7a for the same wind forcing distribution and initial conditions as in Figure 5a (i.e. Eq. 15) and with a drag coefficient γ equals 0.1. This choice of γ along with $\phi_s = 0.3$ yields $2\gamma \sin(\phi_s)(1 + \gamma^2/\sin^2(\phi_s)) = 0.066$. On the other hand, the wind forcing, Eq. (13), with $n = 1$ implies $\tau_\phi(\phi_s) = k\tau_0$ so that for $k = 2$ stability of the fixed point at ϕ_s is granted as long as τ_0 is smaller than its stability cut-off at 0.033. The choice of $\tau_0 = 0.01$, then, puts the expected dynamics well within the stable range of $\tau_0 \in (0.0, 0.033)$ so that, as all three panels of Figure 7a show, the settling of the system into the steady state is very fast. In contrast to this, when τ_0 is set equal to 0.03 (a tad below the stability cut-off at 0.033) the convergence of the trajectory to the fixed point is much slower. As Figure 7b shows, many inertial oscillations take place in this case before the trajectory arrives close to the steady state. When the value of τ_0 is further increased to 0.05—above the stability cut-off value—the fixed point turns unstable as is evident from the results shown in Figure 7c. A careful examination of the system evolution in the 3 panels of Figure 7c supports the analytic considerations: from the middle and lower panels it is evident that the instability of the fixed point is manifested first in the increase of the radius of inertial oscillations, while

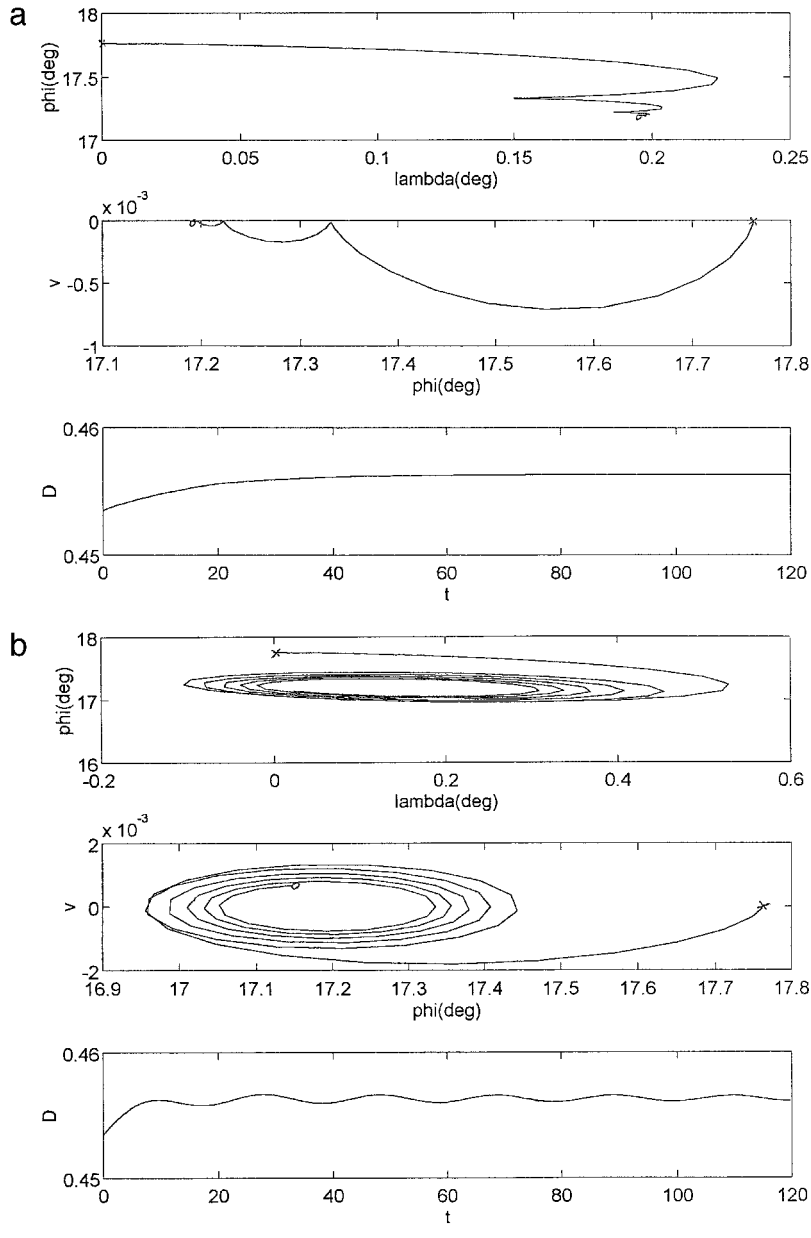

Figure 7. The effect of drag in the vicinity of latitude of vanishing wind forcing for increasing values of the forcing amplitude. The drag coefficient, γ, equals 0.1 and the initial latitude is 0.31 (0.01 Rad. north of $\phi_{ce} = 0.3$). For small amplitude, $\tau_0 = 0.01$ (a), the trajectory settles quickly to the steady state at ϕ_{ce} and D reaches its final value monotonically. As the amplitude is increased, $\tau_0 = 0.03$ (b) the settling to ϕ_{ce} is much slower and D oscillates around its final value. For large enough amplitude, $\tau_0 = 0.05$ (c) the column can be repelled to the equator leaving, altogether, the basin of attraction of ϕ_{ce}.

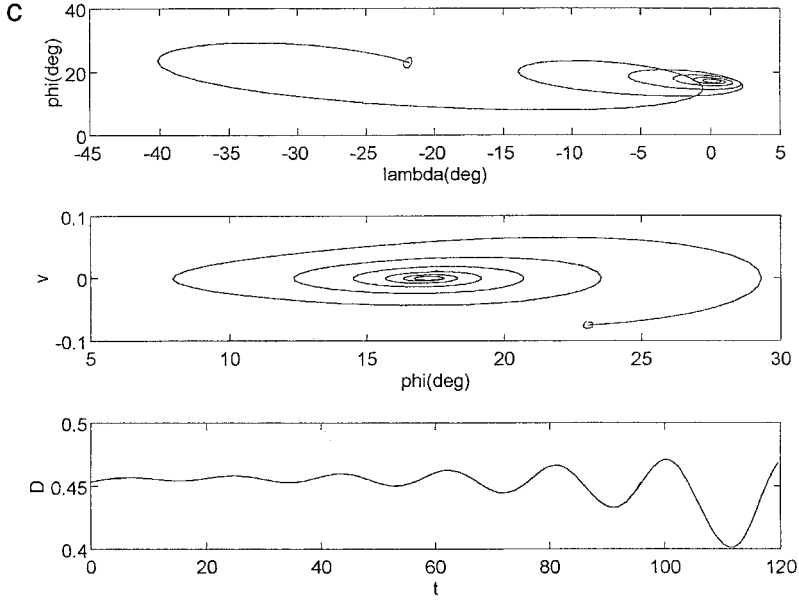

Figure 7.—*Continued*

the value of D during this initial time is hardly altered ($Re\{\eta_{2,3}\}$ is positive while η_1 is negative near the fixed point). When the trajectory reaches latitudes that are far enough from $\phi_s = +0.3$ (by increasing the radius of the inertial oscillations) the direct wind forcing of D (e.g. Eq. 4c) causes large excursions that will eventually cross the Equator.

5. Discussion

The particular parameter values and zonal wind stress form were only chosen in Section 4 to illustrate the expected type of trajectory and not to simulate a particular observation. The role of the various model parameters determining the trajectory that emerges from the preceding analysis and integration is as follows. The initial latitude relative to the fixed point's latitude determines the tendency of the trajectory to move toward or away from the fixed point due to the inertial motion. The form of the wind stress determines the stability of the fixed point according to whether or not the curl of the wind stress also vanishes there. Lastly, drag turns the neutral (elliptic) fixed points into stable ones but does not, necessarily, stabilize the unstable ones.

a. Comparison with f-plane dynamics

The steady transport in the Ekman layer on the f-plane, $\mathbf{V}_e = (\tau x \mathbf{k})/(f)$ (where $\mathbf{k}$—vertical unit vector, τ—wind stress vector and f—the Coriolis parameter), is not a fixed point of the present model since D varies with time following the change in ϕ. Rather than

a fixed point, the steady *f*-plane transport obtains here as a special solution of the drag-free case when $v_t = 0$ (but D and ϕ vary with time). Setting $v_t = 0$ in Eq. (8b) one gets that $D(t) = \frac{1}{2}\cos^2(\phi(t))$ and differentiating this expression with respect to time yields $D_t = -\cos(\phi)\sin(\phi)\phi_t$. Comparing this expression for D_t with that given in Eq. (8c) one gets: $\phi_t \equiv v = -\tau^x(\phi)/\sin(\phi)$ which is precisely the nondimensional form of the Ekman transport on the *f*-plane with $\sin(\phi)$ and $\tau^x(\phi)$ considered constants. Although D is not constant, $u \equiv D/\cos(\phi) - \frac{1}{2}\cos(\phi)$, vanishes at all times so the changes in D induce changes in ϕ only so the kinetic energy is unchanged. Thus, for $\tau = \tau^x$ the north-south, straight line, trajectory on the *f*-plane is trivially transformed into a polar great circle (with constant v) on the Earth.

A meridional wind stress, $\tau = \tau^y$, on the other hand, mandates that $D_t = 0$ (Eq. 8c) and that a τ^y term be added to the right-hand side of Eq. 8b. Setting $v_t = 0$ in Eq. (8b) implies that when τ^y is positive $D > \frac{1}{2}\cos^2(\phi)$ so $u > 0$ and when τ^y is negative $D < \frac{1}{2}\cos^2(\phi)$ so $u < 0$. Thus, for any sign of τ^y, the sign of u in these, $v_t = 0$, solutions of the present model agrees with that on the *f*-plane. However, $v_t = 0$ does not necessarily imply $v = 0$ and when $v \neq 0$ the work done by τ^y on the meridionally moving water column alters its kinetic energy, which will also change the zonal velocity component, in accordance with the temporal change in ϕ when D is conserved. Starting with finite $v(0) = v_0 \neq 0$ the scenario on the Earth is very different from that on the *f*-plane where the addition of an initial, nonzero, velocity component parallel to the wind stress does not entail a subsequent change of the kinetic energy (see Gill, 1982). It can, therefore, be expected that time-dependent wind stress will have a very different effect on the *f*-plane and on the Earth since on the *f*-plane the finite velocity at the time when wind stress changes is simply added to the velocity due to the wind stress itself. By comparison, on the Earth the nonlinear interaction of the two velocities can lead to a decrease/increase in the kinetic energy.

b. Temporal and zonal dependent wind stress

The structure of the dynamical system developed here provides a first step toward analyzing the observed trajectories in the realistic and more complicated cases when the wind forcing is not steady and zonal. A simple illustration of the unexpected effect that a periodic wind stress forcing can have on some of the trajectories calculated above obtains when the expression for the wind forcing in Eq. (13) is simply multiplied by $\sin(\sigma \cdot t)$ where, say, $\sigma = 0.3$. The temporal average of the new wind forcing is zero and it never exceeds the steady forcing (at $t_n = (2n + 1)\pi/2$ the two are equal). The results of the calculations in the two opposing cases corresponding to those shown in Figures 3 and 4 are shown in Figure 8. It is evident from Figure 8a that the oscillatory case of Figure 3 becomes more energetic under the time-dependent forcing with the maximum meridional velocity about 4 times that of the steady forcing. In contrast, the nonoscillatory case of Figure 4, where the drifter traveled 7 degrees of latitude in just 4 days and reached a meridional velocity of 17 m s^{-1}, turned into the oscillatory case of Figure 8b where the latitude span is only 0.6 degree and the meridional velocity is less than 2 m s^{-1}. Thus, time dependence

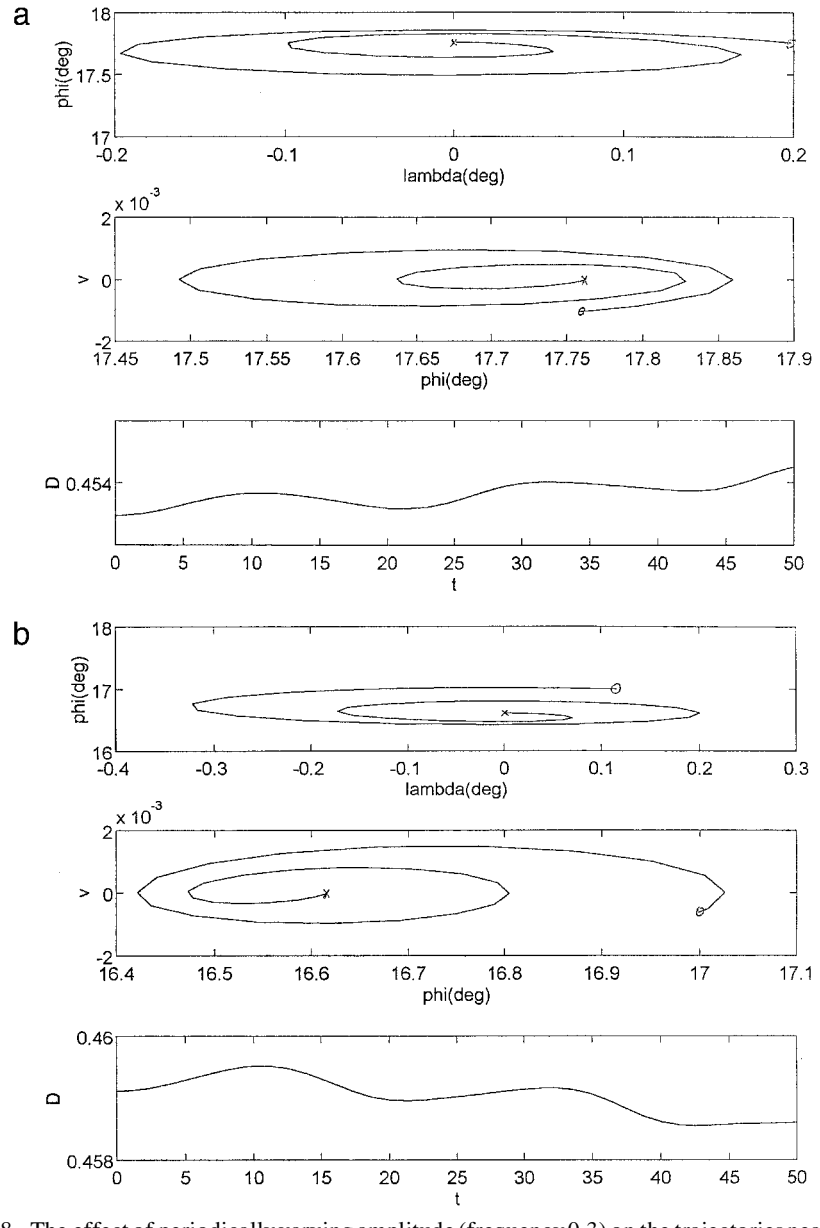

Figure 8. The effect of periodically varying amplitude (frequency 0.3) on the trajectories near ϕ_{ce} in the drag-free cases. (a) Initial latitude located north of the forcing's minimum as in Figure 3. (b) Initial latitude south of the forcing's minimum as in Figure 4. The periodic time dependence implies that the long-term (i.e. at times exceeding several forcing periods) average of the wind forcing is zero although its effect on the trajectories and changes in angular momentum is significant.

interferes with the trajectories of steady wind forcing either constructively or destructively as is expected when a nonlinear system is forced by a periodic forcing. Similar complex effects are encountered when drag is included in the dynamics (not shown) or when zonal variations are included (see below) so one can expect time or zonal variations of the wind stress to alter the steady forcing scenario in a complex way.

Since, in reality the wind stress over the ocean varies with both time and longitude it is expected that both the rate of dispersal of a cluster of drifters and its mean motion are sensitive to the forcing the cluster encounters along its entire trajectory. This might be the reason for the very different trajectories observed when several drifters are launched from nearby locations and for the fast dispersal of drifters that are ubiquitous in observations. A reconstruction of observed trajectories requires both that the stress be known with fine temporal and spatial resolutions and that the available wind fields at a standard height of 10 m are well calibrated with the actual forcing. Both constraints are not likely to be met on a global scale but might be satisfied in regional studies where one can find nearby stations with continuous, long term, wind records.

c. Application to observations

Several points of comparison exist between the (qualitative and quantitative) results of the present model and the observed motion of drogued surface drifters. The first is the angle between the applied wind stress at the ocean's surface and the resulting averaged drifter's trajectory. The present study implies that this angle is highly dependent on the drifter's launching latitude relative to the latitude of zero wind stress. A launch north of that latitude results in an angle of about 90° (Fig. 3) while a launch south of it results in an angle of about 45° (Fig. 4). When the wind stress *curl* does not vanish at that latitude, the resulting scenario is even more complicated (e.g. compare Figs. 5a and 5b). When the wind stress is periodic, rather than steady, many more angles can be expected (e.g. Figs. 8a and 8b). This is consistent with the summary of Niiler and Paduan (1995, Fig. 3) suggesting the existence of a wide range of angles depending on the wind stress frequency but the relationship between the frequency of the wind and the angle is rather complex.

A second observed feature consistent with the results of the present model is the different velocity spectra of two clusters of drifters launched in the NE Pacific under similar wind stress forcing in Oct. 1987 and Oct. 1989 reported by Niiler and Paduan (1995). Despite the similarity in the wind stress spectra in the two years (their Fig. 1), the velocity spectra of the two ensembles of drifters are different, especially at the high frequency (0.5–1 cpd) end (their Fig. 2). The spectral density at the 1 cpd frequency of the 1989 cluster is nearly 100 times higher than that of the 1987 cluster. This conspicuous difference between the two clusters can not be attributed to ensemble size (16 vs. 47 drifters) or duration of drift (6 vs. 3 months) since the wind stress spectra in the two experiments were indistinguishable. Although the authors attribute the difference in spectra to different averaging schemes applied to the two data-sets, the present model

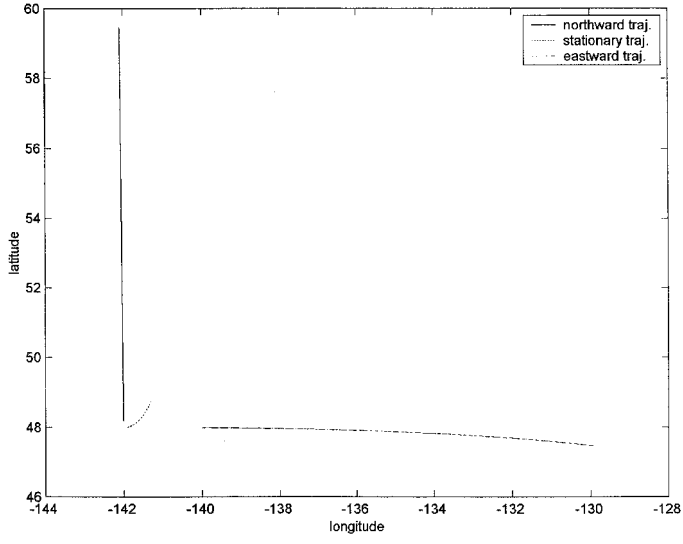

Figure 9. The 164-day-long model-generated trajectories of three numerical drifters launched within 150 km of each other under time-independent and relatively smooth wind stress $-\tau^x(\phi) = \tau_0 \tanh((\phi - 48°)/45°)$, $\tau^y(\lambda) = (0.2\tau_0) \cdot \sin(6(\lambda + 142°))$ with $\tau_0 = -0.0004$. The value of γ is 0.0001 and the initial velocities are: $u(0) = 0 = v(0)$ in all three cases. The launching coordinates of the three trajectories are: $\phi(0) = (48.2°, 48.01°, 47.99°)$; $\lambda(0) = (-142°, -141.9°, -140°)$ for the (northward, stationary and eastward) moving trajectories, respectively. These three trajectories are the numerical counterparts of those shown in Figure 1.

provides an alternate, physical, explanation: Similar (constant) wind stress fields can yield very different velocities and trajectories for drifters launched in slightly different locations. The 5-degree span in central launching location of the two clusters and the difference in their initial spatial distribution are more than sufficient to account for the vastly different spectra even if the wind stress did not change at all between 1987 and 1989. The fact that the biggest spectral gap occurs near the inertial frequency at 1 cpd is consistent with the expectation of the present theory.

Lastly, the present study can account for the fast dispersal shown in Figure 1 with a steady and smooth wind stress. The three trajectories shown in Figure 9 emanate within 100 km of each other and are driven by the steady wind stress: $\tau^x(\phi) = \tau_0 \tanh((\phi - 48°)/45°)$ and $\tau^y(\lambda) = (0.2\tau_0) \sin(6(\lambda + 142°)$ with $\tau_0 = -0.0004$. The quantitative similarity between the trajectories calculated with this wind stress and those shown in Figure 1 points to the significance of nonlinearity included in this model, which merely extends the *f*-plane dynamics to the Earth.

Acknowledgments. This work was supported by the US-Israel Binational Science Foundation via a research grant to HU. I am indebted to A. Mariano of U. of Miami for his helpful comments.

REFERENCES

Böning, C. W. and M. D. Cox. 1988. Particle dispersion and mixing of conservative properties in an eddy-resolving model. J. Phys. Oceanogr., *18,* 320–338.

Dvorkin, Y. and N. Paldor. 1999. Analytical considerations of Lagrangian cross-equatorial flow. J. Atmos. Sci., *56,* 1229–1237.

Figueroa, H. A. and D. B. Olson. 1989. Lagrangian statistics in the South Atlantic as derived from SOS and FGGE drifters. J. Mar. Res., *47,* 525–546.

Gill, A. E. 1982. Atmosphere-Ocean Dynamics, Academic Press Inc., San Diego, CA, 662 pp.

Käse, R. H. and D. J. Olbers. 1979. Wind-driven inertial waves observed during phase III of GATE. Deep-Sea Res., *26,* (Suppl. 1), 191–216.

Kundu, P. K. 1976. An analysis of inertial oscillations observed near Oregon coast. J. Phys. Oceanogr., *6,* 879–893.

Niiler, P. P. and J. D. Paduan. 1995. Wind-driven motions in the northwest Pacific as measured by Lagrangian drifters. J. Phys. Oceanogr., *25,* 2819–2830.

Paduan, J. D. and P. P. Niiler. 1993. Structure of velocity and temperature in the northeast Pacific as measured with Lagrangian drifters. J. Phys. Oceanogr., *23,* 585–600.

Paldor, N. and E. Boss. 1992. Chaotic trajectories of tidally perturbed inertial oscillations. J. Atmos. Sci., *49,* 2306–2318.

Pollard, R. T. and R. C. Millard. 1970. Comparison between observed and simulated wind-generated inertial oscillations. Deep-Sea Res., *17,* 813–821.

Rom-Kedar, V., Y. Dvorkin and N. Paldor. 1997. Chaotic Lagrangian dynamics of particle's horizontal motion in the atmosphere. Physica D., *106,* 389–431.

Received: *8 February, 2001;* revised: *29 October, 2001.*